Investigation of the electrodeposition kinetics of Ni-Mo alloys in the presence of magnetic field

4 AUTHORS, INCLUDING:

Omar Aaboubi
Université de Reims Champagne-Ardenne
64 PUBLICATIONS **595** CITATIONS

SEE PROFILE

Agnieszka Franczak
University of Leuven
12 PUBLICATIONS **35** CITATIONS

SEE PROFILE

Investigation of the electrodeposition kinetics of Ni–Mo alloys in the presence of magnetic field

O. Aaboubi [a,*], A.Y. Ali Omar [a,b], A. Franczak [c], K. Msellak [a]

[a] LISM, UFR Sciences, BP1039, 51687 Reims Cedex 2, France
[b] Universite de Djibouti, BP 1904, Djibouti
[c] Department of Materials Science, Catholic University of Leuven, Kasteslpark Arenberg, 3001 Leuven, Belgium

ARTICLE INFO

ABSTRACT

In the preliminary paper, devoted to the study of magnetic field effects on the catalytic properties of nickel–molybdenum (Ni–Mo) system for hydrogen evolution reaction (HER), we have shown that the main effect of a magnetic field is related to the deposits surface modifications. In the present paper the electrodeposition kinetics of Ni–Mo was investigated, using electrochemical impedance spectroscopy (EIS) and polarization curves methods with and without magnetic fields. The reaction path was proposed to account for the main features of the deposition kinetics (polarization curves and impedance diagrams). This involves the reduction of Ni(II) and Mo(IV) complexed species into compounds that can be included as a whole into the deposit or decomplexed to product alloys deposits. In both cases the charge transfers reactions occurred in more than two steps, coupled by adsorbed intermediates. The proposed model can also account for the current density dependency upon the potential value and the magnetic field intensity.

© 2014 Elsevier B.V. All rights reserved.

1. Introduction

Actually many works have been focused on the preparation and the characterization of catalytic materials with low cost and high catalytic performance to replace the expensive platinum group catalytic materials [1]. It has been shown that alloying nickel with molybdenum improves the catalytic efficiency of nickel during hydrogen evolution reaction (HER) and become the major objective of research during last decays [1–5]. Some of the investigations tackle the complex problem of the Ni–Mo alloys electrodeposition mechanism and several hypotheses have been proposed [6–13]. The proposed mechanism and mathematical model explain certain features of the induced Ni–Mo codeposition and the steady-state behaviors [7].

As it is well known, during electrodeposition process, the application of uniform magnetic field, B parallel to the electrode surface improves the deposit quality (grain size, surface homogeneity and roughness) [14–20]. It was established that the observed effects are attributed to the Lorentz-force-driven convection, i.e. the so-called magnetohydrodynamic (MHD) effect, which introduces additional convection in the electrolytic solution [21–23].

The control process of alloys electrodeposition is engaged with controlling many operating parameters such as bath temperature, pH solution, and chemical composition which are sensitive to the hydrodynamic regime [9]. They include the control of movement or transport of electroactive species from the bulk to the interfacial region. Thus, the use of a superimposed magnetic field should be capable to give further information about the diffusion step of the whole cathodic process. Among the benefits of magneto-convection we found the non-mechanical fluid motion and its application to the micro analysis in small chemical systems for pumping, trapping and transporting, mixing, detection, patterning, sorting, and separation have been found [24]. In addition, the recent development of compact and inexpensive permanent magnets which generally yields strong stirring effects in the electrolytic solution without any external energy input is also under a great interest [25].

In the previous work, we have shown that Ni–Mo alloys electrodeposited under B field exhibits high catalytic performance for HER [4]. The present work is aimed to a better understanding the influence of magnetic field on the Ni–Mo electrodeposition reactions by means of polarization curves and EIS measurements.

2. Experimental conditions

Experiments were performed using a conventional three-electrode set up. The working electrode (WE) was a 5 mm diameter

platinum or 11 mm diameter titanium disk; A large area nickel rod ($A \approx 6$ cm^2) as the counter electrode and a saturated calomel electrode (SCE) as reference electrode has been used. Prior to each experiment, the WE was mechanically polished firstly with emery paper (Struers P 1200 & P 4000), then to a mirror on felt with 1 μm alumina and after rinsed with water and dried. A Ni–Mo predeposit (≈ 2 μm thick) was then plated at potential of $E = -1.2$ vs SCE/V or at constant current density of $j = -35$ mA cm^{-2} for 2 min.

Deionised water was used throughout the experiments. 0.45 M Na$_3$C$_6$H$_5$O$_7$ (Prolabo Normapur), 0.5 M NiSO$_4$, 7H$_2$O (Fluka) and 0.05 M Na$_2$MoO$_4$ (Prolabo) were used for the preparation of the solutions. The pH of the solution was adjusted to 6.2 ± 0.2 by addition of adequate quantities of H$_2$SO$_4$ or NaOH. To avoid some salts precipitation, the bath temperature was maintained at 37 ± 0.5 °C with a thermostat.

The voltammetric experiments were performed with Radiometer (PGZ-100) Potentiostat/Galvanostat equipment controlled by VoltaMaster-4 software. The EIS measurements were carried out using Potentiostat/Galvanostat (Solartron 1286) and a frequency response analyser (Solartron 1250) monitoring by commercial Software Zplot 2.4 (Scribner Associates). The frequency range examined here lies from 65 kHz to 5 or 1 mHz and to get the EIS measurements in the linear mode, a sine wave potential amplitude of $\Delta E = 10$ mV was used. In all case, the measurements were repeated more than two times and an acceptable reproducibility was obtained.

For the measurements with magnetic field, the cell was put into the gap of an electromagnet (SIGMA-PHI) coupled with a regular power supply (BOUHNIK). The magnet can generate a homogeneous magnetic field up to 1.2 T for 7 cm gap and 1.65 T for 5 cm gap. The working electrode was positioned in the electrochemical cell, near the center of pole pieces.

3. Results

3.1. Polarization curves

The polarization curves were measured with and without magnetic field, using cyclic voltammetry at low potential scan rate. The influence of field was examined when the electrode surface was oriented in the horizontal downward position (Fig. 1) and in the vertical position (Fig. 2). It has been determined that the effect of the B field does not depend on the electrode orientation. In all cases an increase of the electrolytic current was observed. In the other hand, with horizontal electrode (Fig. 1), the polarization curves

exhibit some current oscillations at high potential level and decrease significantly when the field is applied. This may be due to the hydrogen bubbles that longer remain attached to the electrode surface when it is in horizontal facing downward position. According to the previous works, when the B field is applied perpendicular to the current density lines the Lorentz force takes place in the third direction generating a solution flow tangentially to the electrode. Consequently, the hydrogen bubbles detachment is significantly facilitated leading to an active surface more accessible [23]. In the case of vertically positioned electrode, practically no current oscillations are visible (Fig. 2). The combination of natural and MHD convection induces easier H$_2$ bubbles releasing. To avoid the problem of bubbles evolution during deposition process the working electrode was placed in vertical position. It is worth noting that either with or without magnetic field, the presence of Ni–Mo alloy deposit on the substrate, catalysts the HER occurring at more negative polarization potentials.

Chemical composition of the Ni–Mo alloys deposited at constant current density of $j = -35$ mA cm^{-2} for 30 min has been obtained using energy-dispersive X-ray (EDX) analysis. In Table 1 we have reported the experimental values of Ni at.% and Mo at.% measured at various magnetic field strength. In both cases the alloy composition is practically the same with or without magnetic field, what is also reported in [4,18].

According to the previous works [21–23], under MHD convection control, the current density, j, is proportional to $B^{1/3}$. Fig. 3A indicates the relation of j vs $B^{1/3}$ for some polarization values. As it can be seen, for B field higher than 0.4 T straight lines are obtained when polarization is more negative than $E = -1.20$ vs SCE/V. Using linear regression method, the following relationship (Eq. (1)) may be obtained

$$j(B, E) = \kappa_1 B^{1/3} + \kappa_2 \tag{1}$$

and the values of the slope κ_1 show a typical Tafel evolution at low potential value

$$\kappa_1 = \kappa_{10} \exp[bE] \tag{2}$$

where b has V^{-1} unit, κ_{10} is the pre-exponential term and the parameter κ_2 has linear dependency upon the potential values. Fig. 3B reports the evolution of log($-\kappa_1$) upon potential value, E. The data show a linear evolution followed by a limiting value for $E < -1.30$ vs SCE/V. This indicates that at low potential value, the Ni–Mo alloys deposition is under mixed regime (mass transport and kinetic controls).
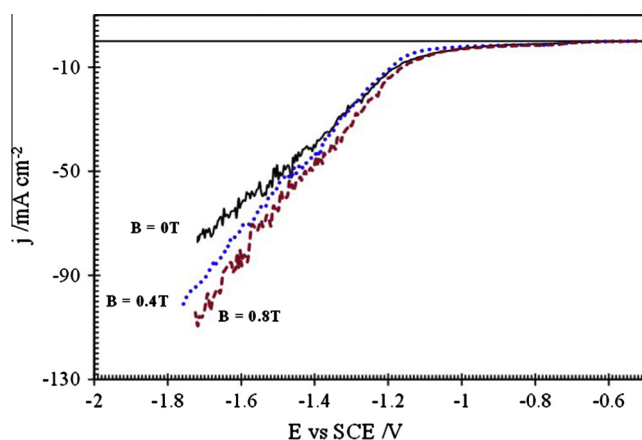
Fig. 1. Polarization curves measured on horizontal Pt disk electrode with increasing magnetic field values. [NiSO$_4$] = 0.50 mol dm^{-3}; [Na$_2$MoO$_4$] = 0.05 mol dm^{-3}; [Na$_3$C$_6$H$_5$O$_7$] = 0.45 mol dm^{-3}; v = 0.25 mV s^{-1}; pH = 6.2; T_b = 37 °C.
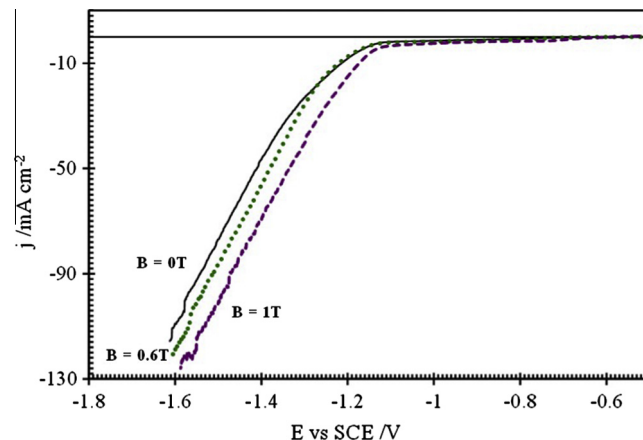
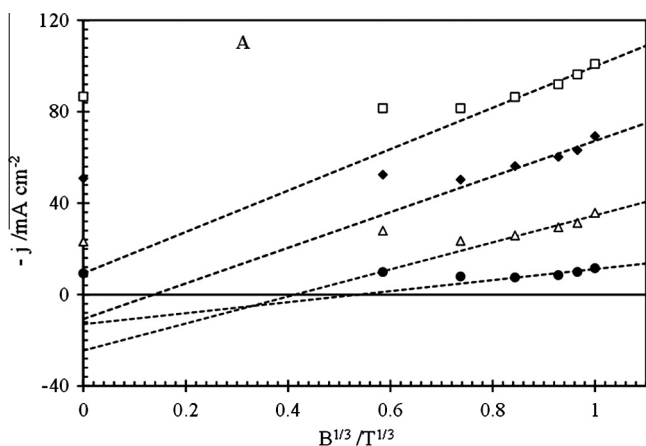

Fig. 2. Polarization curves measured on vertical Pt disk electrode with increasing magnetic field values. [NiSO$_4$] = 0.50 mol dm^{-3}; [Na$_2$MoO$_4$] = 0.05 mol dm^{-3}; [Na$_3$C$_6$H$_5$O$_7$] = 0.45 mol dm^{-3}; v = 0.25 mV s^{-1}; pH = 6.2; T_b = 37 °C.
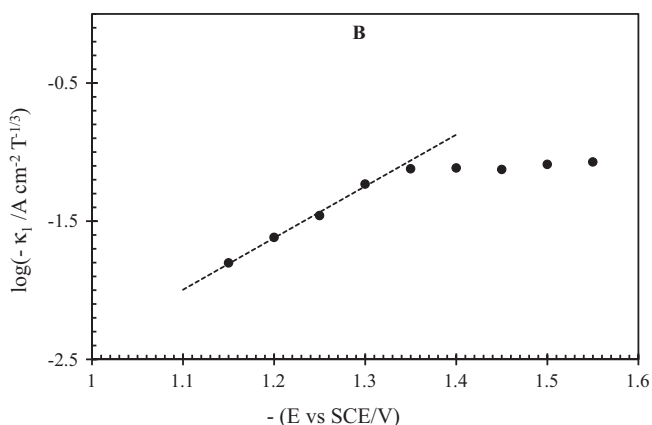
Table 1
Nickel and molybdenum content deduced from the EDX analysis of deposit obtained under various applied magnetic field intensities.

| B (T)	Ni (at.%)	Mo (at.%)
0	73 ± 3	27 ± 3
0.5	74 ± 8	26 ± 8
1	74 ± 4	26 ± 4

Fig. 3A. Current density $-j$ vs $B^{1/3}$ measured on vertical Pt disk electrode with increasing cathodic polarization: (●): $E = -1.20$ vs SCE/V; (△): $E = -1.3$ vs SCE/V; (◆): $E = -1.4$ vs SCE/V; (□): $E = -1.5$ vs SCE/V.


Fig. 3B. Potential dependence of $\log(-\kappa_1)$ for vertical Pt disk electrode. κ_1 data are calculated from linear part of $-j$ vs $B^{1/3}$ in Fig. 3A.

3.2. Electrochemical impedance spectroscopy (EIS)

Electrochemical impedance spectroscopy (EIS) is an excellent technique for studying reaction mechanisms and kinetics. Based on disruption method, this technique is able to probing relaxation processes over a large frequency domain. The EIS studies have been carried out at various potential values and various magnetic field intensities up to 0.9 T. The impedance diagrams depend mainly on the polarization values and the magnetic field intensity (Figs. 4A and B). The diagrams exhibit two collapsed capacitive features without matter whether the process was under or without field, that are then followed by an inductive response, strongly dependent on polarization level (Figs. 4A and B). At fixed polarization and in the low frequency range an additional capacitive loop was observed and its amplitude was influenced by B field intensity (Fig. 5). Although the Warburg impedance does not appear here,
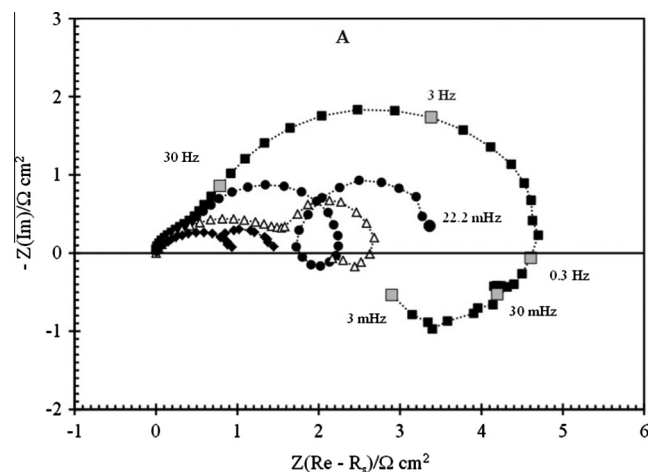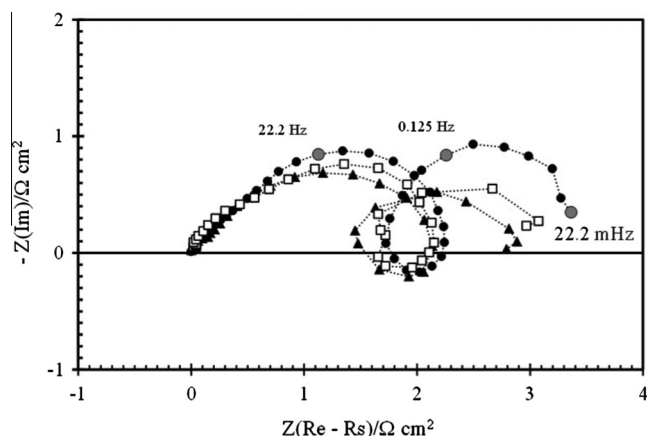

Fig. 4A. Nyquist plot of typical EIS diagrams for vertical Pt disk electrode measured without magnetic field. [Na₂MoO₄] = 0.05 M; [NiSO₄] = 0.5 M & [Na₃C₆H₅O₇] = 0.45 M. pH = 6.2 & T_b = 37 °C. The electrolyte resistance, R_s, has been subtracted. (■) $E = -1.10$ vs SCE/V; (●) $E = -1.20$ vs SCE/V; (△) $E = -1.30$ vs SCE/V; (◆) $E = -1.40$ vs SCE/V.
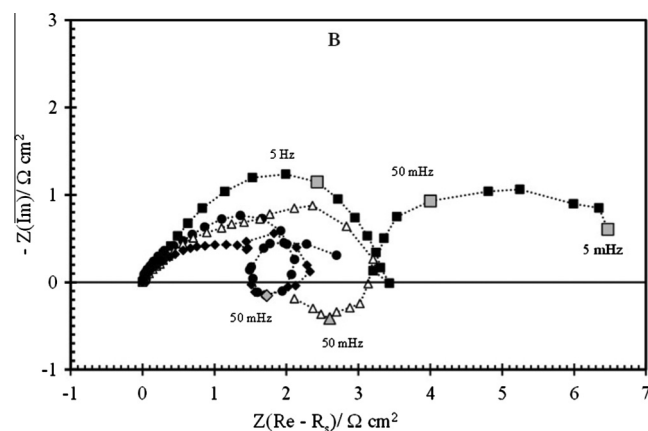
Fig. 4B. Nyquist plot of typical EIS diagrams for vertical Pt disk electrode measured with magnetic field. B = 0.75 T. [Na₂MoO₄] = 0.05 M; [NiSO₄] = 0.5 M & [Na₃C₆H₅O₇] = 0.45 M. pH = 6.2 & T_b = 37 °C. The electrolyte resistance, R_s, has been subtracted. (■) $E = -1.10$ V/SCE; (●) $E = -1.20$ vs SCE/V; (△) $E = -1.30$ vs SCE/V; (◆) $E = -1.40$ vs SCE/V.

this loop may be associated with the diffusion process which occurs in this polarization region. For potential more negative then $E = -1.20$ vs SCE/V, in addition to the mentioned capacitive loop, there is a second inductive feature appearing with an apex frequency typically around 50 mHz and an amplitude more pronounced under magnetic field conditions (see Fig. 4B). At high polarization level only the capacitive loops are visible.

Fitting procedure was applied using commercial software ZSimpWin 3.21 (EChem Software) and the equivalent circuit depicted in Fig. 6. The values of a solution resistance R_s, the charge transfer resistance R_{ct}, and the double layer capacity C_{dl}, have been determined from the small high frequency loop. The characteristic parameters of the second medium frequency feature: R_1 and Q_1 were also obtained and attributed to the capacitive relaxation type of adsorbed species. Taking into account the surface imperfection problems, a phase constant element (CPE) instead of a pure capacitance [26–28] have been introduced in the fitting procedure. Therefore, the capacitance values can be obtained through the expression of the time constant described by the impedance, Z_{HF} expressed as follow

Fig. 5. Nyquist plot of typical EIS diagrams measured at constant potential $E = -1.20$ vs SCE/V with increasing magnetic field values. [Na$_2$MoO$_4$] = 0.05 M; [NiSO$_4$] = 0.5 M & [Na$_3$C$_6$H$_5$O$_7$] = 0.45 M. pH = 6.2 & T_b = 37 °C. The electrolyte resistance, R_s, has been subtracted. (●) B = 0; (□) B = 0.6 T; (▲) B = 0.9 T.
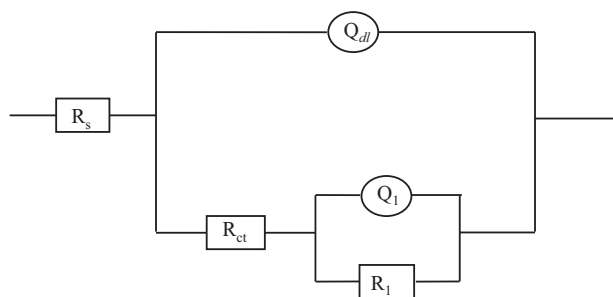
Fig. 6. Equivalent circuit used for the EIS experimental data fitting. R_s is the solution resistance, R_{ct} is the charge transfer resistance and typical CPE elements respectively related to the high frequency capacitive loop (R_{ct}, Q_{dl}) and to the middle frequency capacitive loop: (Q_1, R_1).

$$Z_{HF} = R_s + R_{ct}/[1 + (i\omega R_{ct} \cdot C_{dl})^\beta] \qquad (3)$$

where $i^2 = -1$ and β is the CPE exponent [26–28]. To check the stability of our system, the measurements have been tested using Kramers–Kronig transformation (the so-called KK-test) [27]. Only the frequency range for which the residual errors were less than 1% was selected.

3.2.1. Double layer capacitance

From the fitting data, the values of each capacitance element, C_{dl} and C_1, have been calculated according to the formula proposed by Brug et al. [26]. In the case of C_{dl} element the latter can be expressed as follow

$$C_{dl}^\beta = Q_{dl}/(R_s^{-1} + R_{ct}^{-1})^{1-\beta} \qquad (4)$$

Fig. 7A shows the potential variation of the double layer capacitance, C_{dl}, obtained without and with B = 0.75 T. From the figure, an increase of C_{dl} values with magnetic field is observed. The increase of C_{dl} may be attributed to modification of real surface area due to the modification of the porosity and roughness of the Ni–Mo deposits surface [4]. In fact, during the Ni–Mo electrodeposition, a part of the current is consumed by the hydrogen evolution reaction which may considerably increase when the co-discharge of molybdenum occurs due to low hydrogen overvoltage on the Mo alloy [29]. Consequently the local pH increases near the electrode and the nodular morphology of deposited films is promoted due to basic pH values [6]. Both reactions are influenced by hydrodynamic conditions. Hence, with presence of magnetic convection the Ni–Mo deposits
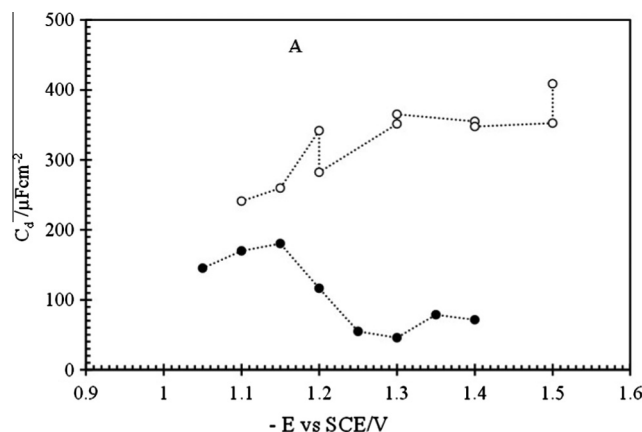
Fig. 7A. Potential dependence of C_{dl} capacitance calculated from the fitting data and Eq. (4). Vertical Pt electrode: (●): B = 0; (○): B = 0.75 T. [Na$_2$MoO$_4$] = 0.05 M; [NiSO$_4$] = 0.5 M & [Na$_3$C$_6$H$_5$O$_7$] = 0.45 M. pH = 6.2 & T_b = 37 °C.

become quite amorphous with some holes and large agglomerations of typical nodular grains [4]. It appears that B field acts indirectly on the Ni–Mo deposits morphology through the perturbation of secondary processes, namely, the hydrogen evolution, molybdenum reduction and the inhibitor adsorption [14].
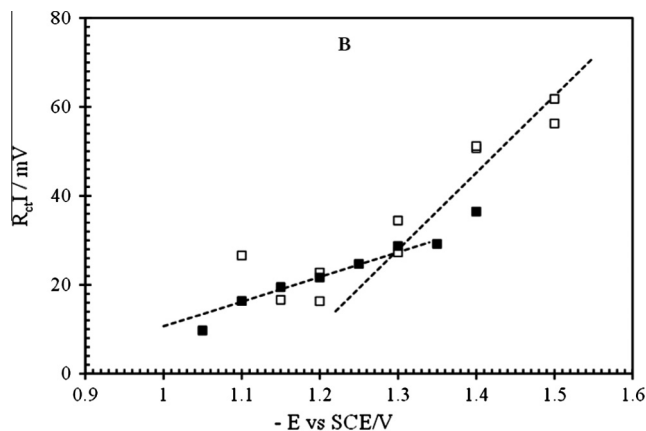
3.2.2. Charge transfer resistance

Fig. 7B represents the product of charge transfer resistance by the current intensity $R_{ct}I$, against the polarization potential for B = 0 and B = 0.75 T, respectively. Despite the dispersion of R_{ct} and I values, with or without magnetic field, same straight lines are observed. Similarly as in [30,31], no magnetic field effects on the charge transfer process may be also here characterized. For low polarization values, the product $R_{ct}I$ vs E exhibits a first slope of 55 mV/V over 250 mV potential range (i.e. −1.25 vs V/SCE ⩽ E ⩽ −1.05 vs V/SCE) and a linear increase with a slope of 156 mV/V, for higher cathodic polarization. The potential variation of $R_{ct}I$ product is consistent with the work of Chassaing et al. [6]. The presence of two slopes indicates that more than two reactions occur during Ni–Mo alloys deposition process [10].

4. Theory

### 4.1. Reactions mechanisms

Many investigations have been devoted to Ni–Mo alloys electrodeposition from citric bath under various pH conditions

Fig. 7B. Potential dependence of $R_{ct}I$ product (charges transfer resistance × current). Vertical Pt electrode: (●): B = 0; (○): B = 0.75 T. [Na$_2$MoO$_4$] = 0.05 M; [NiSO$_4$] = 0.5 M & [Na$_3$C$_6$H$_5$O$_7$] = 0.45 M. pH = 6.2 & T_b = 37 °C.
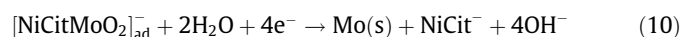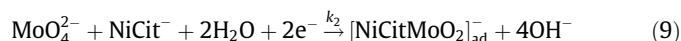
[9] and several hypothesis have been proposed to elucidate the reactions mechanism of its co-deposition kinetics [6,7,10,12]. Based on thermodynamic data, Auger electron spectroscopy (EAS) and EDX analysis, Chassaing et al. [6] explained the MoO_2 layer formation and Ni_3Mo formula of the obtained deposit, proposing the following reactions mechanism

$$MoO_4^{2-} + 2H_2O + 2e^- \rightarrow MoO_2 + 4OH^- \tag{5}$$

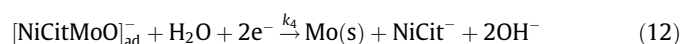$$MoO_2 + 4Ni^{2+} + 8e^- \leftrightarrows MoO_2Ni_4 \tag{6}$$
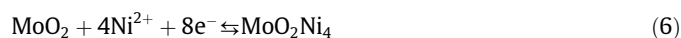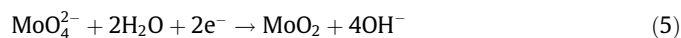
The authors consider that the global reaction leading to the alloy deposit formula Ni_3Mo involves hydrogen inclusion according to the following

$$MoO_4^{2-} + 4Ni^{2+} + 8e^- + (4+n)H \rightarrow MoNi_3 + 4OH^- + nH_{included} \tag{7}$$
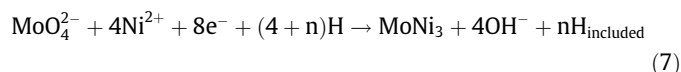
To predict the behavior of induced Ni–Mo codeposition, Podlaha et al. [7] developed a mathematical model based on reactions mechanism involving an adsorbed intermediate where molybdenum is in +IV state and for which the formula $[NiCitMoO_2]_{ad}^-$ has been proposed. Its reduction leads to the complexed Ni(II) and Mo(s) in metallic state. The following reaction mechanism has been assumed [7]

$$NiCit^- + 2e^- \xrightarrow{k_1} Ni(s) + Cit^{3-} \tag{8}$$

$$MoO_4^{2-} + NiCit^- + 2H_2O + 2e^- \xrightarrow{k_2} [NiCitMoO_2]_{ad}^- + 4OH^- \tag{9}$$

$$[NiCitMoO_2]_{ad}^- + 2H_2O + 4e^- \rightarrow Mo(s) + NiCit^- + 4OH^- \tag{10}$$

Based on above, the authors indicate that molybdenum can be deposited only from the adsorbed intermediate and nickel deposition proceeds independently on molybdenum. The proposed mathematical model gives helpful explanation of the steady state data. Nevertheless regarding the number of time constant appearing in the EIS diagrams, more than three in certain cases, it is difficult to relate that to the relaxations of only adsorbed $[NiCitMoO_2]_{ad}^-$ involving in Eqs. (9) and (10). Thus, we assume that $[NiCitMoO_2]_{ad}^-$ leads to appearance of another adsorbed intermediate $[NiCitMoO]_{ad}^-$, where molybdenum is in the +II state accordingly with the following reactions

$$[NiCitMoO_2]_{ad}^- + H_2O + 2e^- \xrightarrow{k_3} [NiCitMoO]_{ad}^- + 2OH^- \tag{11}$$

$$[NiCitMoO]_{ad}^- + H_2O + 2e^- \xrightarrow{k_4} Mo(s) + NiCit^- + 2OH^- \tag{12}$$

$$H_2O + 2e^- \xrightarrow{k} 1/2H_2 + OH^- \tag{13}$$

Regarding [7], the water reduction reaction which leads to the hydrogen formation can be considered as the side reaction (Eq. (13)) and it takes place at the free adsorption part of the surface.

4.2. Steady state current density

We can assume that each intermediate specie, is identically adsorbed at the available surface sites according to Langmuir isotherm type. The surface ratio recovered by $[NiCitMoO_2]_{ad}^-$ and $[NiCitMoO]_{ad}^-$ are θ_1 and θ_2, respectively; Γ is the number of maximum available sites per surface unit and C_1 and C_2 are the surface concentration of $NiCit^-$ and MoO_4^{2-} ions, respectively. The reactions Eqs. (8), (9), (11) and (12) follow Tafel activation with potential and their rate constants are expressed as

$$k_i = k_i^\circ \exp[b_i(E - E_0)] \tag{14}$$

where b_i and k_i° are the Tafel slope and pre-exponential constant of each reaction, respectively. The latter corresponds to the rate

constant at the open circuit potential (OCP) value, E_0. Then, the current density j, is given by

$$j = -2F[(K_1 + K_2)(1 - \theta_1 - \theta_2) + K_3\theta_1 + K_4\theta_2] \tag{15}$$

and the formation/destruction rates of each intermediate specie is respectively given by

$$\Gamma(d\theta_1/dt) = K_2(1 - \theta_1 - \theta_2) - K_3\theta_1 \tag{16}$$

$$\Gamma(d\theta_2/dt) = K_3\theta_1 - K_4\theta_2 \tag{17}$$

At the steady state the above terms must be zero and the fractional surface coverage are

$$\theta_1 = \frac{K_2K_4}{N}; \quad \theta_2 = \frac{K_2K_3}{N} \quad \text{and} \quad 1 - \theta_1 - \theta_2 = \frac{K_3K_4}{N} \tag{18}$$

where $N = K_2K_4 + K_3(K_2 + K_4)$ and $K_1 = k_1C_1$, $K_2 = k_2C_1C_2$, $K_3 = k_3\Gamma$, $K_4 = k_4\Gamma$, $K = k/2$ and F is the Faraday constant. Hence the stationary current density is given by

$$j = -2F\frac{K_3K_4(K_1 + 3K_2 + K)}{K_2K_4 + K_3(K_2 + K_4)} \tag{19}$$

In Eq. (19) the values of K_1 and K_2 are very sensitive to the hydrodynamic conditions which may modify the concentration profiles near the electrode surface. The hydrodynamic conditions may be controlled using various setups such as rotating disk electrode (RDE) [6], rotating cylinder [7] or using magnetic convection as in our previous works [4,18]. In fact at a distance y from the electrode, for each species, i, the concentration C_i of each specie i, is given by Fick's second law

$$\frac{\partial C_i}{\partial t} = D_i \frac{\partial^2 C_i}{\partial y^2} \tag{20}$$

where D_i is the diffusion coefficient of i. In the case of boundary conditions for a Nernst diffusion layer of thickness δ_i, the concentration C_i is equal to

$$C_i(y) = C_i + (C_i^* - C_i)(y/\delta_i) \text{ for } y < \delta_i \tag{21}$$

$$C_i(y) = C_i^* \text{ for } y \geqslant \delta_i \tag{22}$$

where C_i^* is the bulk concentration of diffusing specie i.

In our case the bulk concentration of Ni(II) ions, C_1^*, is much higher than the bulk concentration C^*, of MoO_4^{2-} ions. In addition, Landolt et al. [7,8] and Beltowska-Lehman et al. [9] have shown that in such conditions only the reduction of Mo(VI) ions are under mass transport control. Moreover, if we assume that all the citrate is complexed with nickel ions [6,7] then $C_1 \approx C_1^* = C(NiCit^-)^*$. We set also $m = D/\delta$ as the Mo(VI) ions mass transport coefficient. In this case the surface concentration, $C_2 = C = C(MoO_4^{2-})$, of such species in the solution is of the following relationship

$$\frac{-k_2C_1^*CK_3K_4}{k_2C_1^*C(K_3 + K_4) + K_3K_4} = m(C - C^*) \tag{23}$$

Obviously, Eq. (23) leads to a quadratic equation which can be linearized and easily solved, using approximations as follow

$$\frac{k_2C_1^*C}{1 + (k_2C_1^*C/K_0)} = m(C^* - C) \tag{24}$$

In Eq. (24), the term K_0 corresponds to

$$K_0 = \frac{K_3K_4}{(K_3 + K_4)} \tag{25}$$

We can assume that $k_2C_1^*C/K_0 \ll 1$, what may be verified in a whole potential range. For example, taking into account the values reported in Table 2, if $(E - E_0) = -5$ mV then

$k_2 C_1^* C^*/K_0 = 5.719 \times 10^{-4}$. However for $(E - E_0) = -1$ V this term reaches only $k_2 C_1^* C^*/K_0 = 9.828 \times 10^{-2}$. In this case, the concentration evolution against the polarization value is given by

$$C = \frac{C^*}{1 + \left(\frac{k_2^\circ}{m} \exp\left[b_2(E - E_0)\right]\right)} \qquad (26)$$

It can be observed in Fig. 8 that under applied magnetic field the surface concentration for a large potential range remains at high level.

As the matter of fact, without magnetic field the diffusion layer thickness, δ, at the vertical oriented electrode is controlled by the natural convection [32,33]. Its dependency expression upon the concentration, C^*, can be obtained using the classical limiting current equation in Nernst layer assumption and the limiting current expression given in [32,33]. For circular electrode with diameter d, the diffusion layer thickness δ is given by

$$\delta = 1.44 \frac{d^{1/4} D^{1/4}}{\left(\frac{g}{v} \alpha_0 C^*\right)^{1/4}} \qquad (27)$$

where α_0 is the specific densification coefficient, g is the gravity acceleration and v stands for kinematic viscosity.

Nevertheless, with a magnetic field, the δ evolution upon B field can be obtained using the same calculation procedure, leading to [23]

$$\delta = 1.16 \frac{d^{1/3} D^{1/3}}{(\kappa B C^*)^{1/3}} \qquad (28)$$

where κ is an experimental constant defined in [23] and which depends on the fluid viscosity [34].

4.3. Electrochemical impedance

As a small sine wave potential perturbation is superimposed to the stationary polarization point, a sine wave modulation, $\Delta\theta_i$ and ΔC_i are produced. The faradic impedance by surface unit, Z_F, is given by

$$Z_F^{-1} = \left(\frac{\partial j}{\partial E}\right) + \left(\frac{\partial j}{\partial \theta_1}\right)\frac{\Delta\theta_1}{\Delta E} + \left(\frac{\partial j}{\partial \theta_2}\right)\frac{\Delta\theta_2}{\Delta E} + \sum_i \left(\frac{\partial j}{\partial C_i}\right)\frac{\Delta C_i}{\Delta E} \qquad (29)$$

where the charge transfer resistance, R_{ct} corresponds to

$$R_{ct}^{-1} = \left(\frac{\partial j}{\partial E}\right) = \frac{2F}{N}\left[(b_1 K_1 + bK) + K_2(b_2 + b_3 + b_4)\right] \qquad (30)$$

$$\left(\frac{\partial j}{\partial \theta_1}\right) = 2F(K_1 + K_2 - K_3 + K) \qquad (31)$$

Table 2
Values of the different characteristic parameters used for polarization curves and EIS diagrams simulations.

B (T)	0	0.75	1
b_1 (V^{-1})	-10.6	-11.7	-11.8
b_2 (V^{-1})	-7.90	-7.90	-7.90
b_3 (V^{-1})	-2.68	-2.20	-2.20
b_4 (V^{-1})	-2.70	-2.80	-2.80
b (V^{-1})	-12.5	-12.5	-12.5
k_1° (cm s^{-1})	8.70×10^{-2}	0.11	0.15
k_2° (cm^4 mol^{-1} s^{-1})	3.65×10^{-4}	5.35×10^{-4}	6.35×10^{-4}
k_3° (cm s^{-1})	6.05×10^{-7}	4.50×10^{-7}	4.50×10^{-7}
k_4° (cm s^{-1})	2.55×10^{-9}	2.55×10^{-9}	2.55×10^{-9}
k° (cm^4 mol^{-1} s^{-1})	1.35×10^{-13}	1.45×10^{-13}	1.45×10^{-13}
Γ (mol cm^{-2})	2.6×10^{-9}	2.5×10^{-9}	2.5×10^{-9}
m (cm s^{-1})	9.43×10^{-4}	2.09×10^{-3}	2.63×10^{-3}
D (cm^2 s^{-1})	1.0×10^{-5}	1.0×10^{-5}	1.0×10^{-5}
δ (cm)	1.06×10^{-2}	4.78×10^{-3}	3.80×10^{-3}
R_s (Ω cm^2)	2.55	2.67	2.96
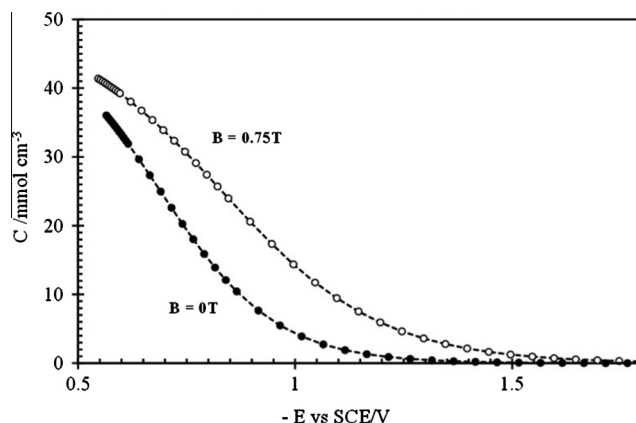
Fig. 8. Potential dependence of calculated surface concentration according to Eq. (26) and the parameters values depicted in Table 2.

$$\left(\frac{\partial j}{\partial \theta_2}\right) = 2F(K_1 + K_2 - K_4 + K) \qquad (32)$$

$$\frac{\Delta\theta_1}{\Delta E} = \frac{K_2 K_3 K_4 (b_2 - b_3)}{(i\omega\Gamma + K_2 + K_3)N} \qquad (33)$$

$$\frac{\Delta\theta_2}{\Delta E} = \frac{K_2 K_3 K_4 (b_3 - b_4)}{(i\omega\Gamma + K_4)N} \qquad (34)$$

where $\omega = 2\pi f$ is the pulsation and f is the frequency. In addition, the admittance term corresponding to the concentration modulation is

$$\sum_i \left(\frac{\partial j}{\partial C_i}\right)\frac{\Delta C_i}{\Delta E} = \sum_i \frac{R_{ct}}{nFD_i}\frac{\Delta C_i(y=0)}{\left(\frac{\partial\Delta C_i}{\partial y}\right)_{y=0}} \qquad (35)$$

Hence the total faradic admittance can be expressed as the sum of four terms

$$Z_F^{-1} = R_{ct}^{-1} + Z_1^{-1} + Z_2^{-1} + Z_d^{-1} \qquad (36)$$

in which Z_1 and Z_2 may be respectively expressed as follow

$$Z_1^{-1} = \frac{1/\rho_1}{(i\omega + 1/\tau_1)} \quad \text{and} \quad Z_2^{-1} = \frac{1/\rho_2}{(i\omega + 1/\tau_2)} \qquad (37)$$

wherein

$$\rho_1^{-1} = \frac{2F}{\Gamma} \frac{(K_2 K_3 K_4)[(b_2 - b_3)(K_1 + K_2 - K_3)]}{[K_1(K_2 + K_3) + K_3(K_2 + K_4)]} \qquad (38)$$

$$\tau_1^{-1} = \frac{K_2 + K_3}{\Gamma} \qquad (39)$$

$$\rho_2^{-1} = \frac{2F}{\Gamma} \frac{K_2 K_3 K_4 (K_1 + K_2 - K_4)[(b_3 - b_4)]}{[K_2 K_4 + K_2 K_3 + K_3 K_4]} \qquad (40)$$

$$\tau_2^{-1} = \frac{K_4}{\Gamma} \qquad (41)$$

The diffusion impedance Z_d corresponds to

$$Z_d = \sum_i \frac{R_{ct}}{nFD_i}\frac{\Delta C_i(y=0)}{\left(\frac{\partial\Delta C_i}{\partial y}\right)_{y=0}} \qquad (42)$$

In the case of disk electrode maintained in vertical position without imposition of magnetic field, the algebraic representation of the diffusion impedance Z_d, has been previously established by Citti et al. [35] in term of the dimensionless frequency

$$\sigma_i = \frac{\omega \delta_i^2}{D_i} \tag{43}$$

Under magnetic field conditions and by use of same calculation methods, Devos et al. [36] proposed a general algebraic representation of Z_d in term of dimensionless frequency σ_i for each diffusing specie i.

In general, for electrochemical step under mixed kinetic and mass transport control the relationship between charge transfer resistance and magnetic field may be established as follow. For each step i the current density and the concentration at the electrode surface are

$$j = -nFk_iC \quad \text{and} \quad C = C^*(1 - j/j_l) \tag{44}$$

where j_l corresponds to the diffusion limiting current density. Knowing that at each polarization point R_{ct} corresponds to the slope of the E–j relationship, according to Eq. (30), the following can be established

$$R_{ct} = \frac{1}{nF\left(\frac{\partial k_i}{\partial E}\right)C^*} + \frac{1}{j_l}\frac{k_i}{\left(\frac{\partial k_i}{\partial E}\right)} \tag{45}$$

As the rate constant k_i is Tafels' activation form (Eq. (14)), Eq. (45) may be written in the following form

$$R_{ct} = \frac{1}{nFC^*b_ik_i} + \frac{1}{b_ij_l} \tag{46}$$

According to [23] the current density j_l is given by

$$j_l = 0.864nFD^{2/3}C^*(\kappa C^*B)^{1/3}d^{-1/3} \tag{47}$$

this leads to

$$R_{ct} = \frac{1}{nFC^*b_ik_i} + \frac{1}{0.864nFb_iC^*D^{2/3}(\kappa C^*B)^{1/3}d^{-1/3}} \tag{48}$$

It must be noticed that in Eq. (48) the charge transfer resistance is the sum of two terms where the first one corresponds to the charge transfer component which does not depend of magnetic field and the second term may be attributed to the mass transport contribution, presenting a linear evolution vs $B^{-1/3}$.

The total impedance is calculated taking account the double layer capacitance C_{dl}, which is parallel to the faradic Z_F.

In the complex plot, shape of the impedance diagrams may be deduced thorough the examination of the signs of ρ_1 and ρ_2 parameters. In general, there are two capacitive loops in the complex plan followed or separated by a partial diffusion loop, and by inductive loop at low frequency. Generally the high frequency loop is related with the charge transfer resistance in parallel with double layer capacitance. The medium frequency capacitive loop is associated with the capacitive relaxation of adsorbed intermediate, (namely when $\rho_1 < 0$) and the low frequency loop which appears in the negative part of the complex plan, is related with the inductive relaxation of adsorbed intermediate (namely when $\rho_2 > 0$).

5. Discussion

5.1. Polarization curves

In Fig. 9 the experimental polarization curves are compared with that calculated using Eq. (19) and values reported in Table 2. With or without magnetic field the comparison displays a good accordance between experimental and calculated data. The data reported in Table 2 show that under B field the best accordance is obtained with high values of $k_1°$ and $k_2°$ and low value of diffusion layer thickness, δ. In fact, lowering δ is in accordance with the MHD convection generated near the electrode surface when B field is applied. According to Eq. (28) when B increases the thickness δ

decreases in the form of $B^{-1/3}$. However the fact that $k_1°$ and $k_2°$ varied with B field indicates that the steps (1) and (2) are sensitive to the hydrodynamic conditions through the diffusion from the electrode surface to the bulk of Cit^{3-} and OH^- released species [36]. It is worth noting that for the cathodic low polarization the calculated curves seem to be not in accordance with the experimental ones. In fact, as it was noted above in this potential region the MoO_2 oxide layer formation, is promoted according to Eq. (5). In addition, in the previous work [37] we have shown that in the case of citrate bath without Ni and Mo, the citrate ions would be reduced by releasing the labile hydrogen of the alcohol function [6] and cathodic vague was measured [37]. The observed discrepancy could be due to the fact that the calculated model does not take into consideration such reactions.

5.2. Electrochemical impedance diagrams

As for the polarization curves a similar conclusion may be drawn when comparing the experimental EIS data to the calculated ones, using Eqs. (3) and (36). Fig. 10 indicates the experimental impedance diagrams together with the calculated from the model, using the parameter values depicted in Table 2. The results show that the experimental diagrams are well represented and that our assumption can be considered to account for the experimental data.

From the experimental high and middle frequency loops we have obtained already described above, fitted values of R_{ct}, C_{dl}, R_1 and C_1. Now one can construct the corresponding equivalent electrical circuit (EEC) based on Fig. 11 where only pure electric elements are considered and for which the impedance, Z_1, can be expressed as follow

$$Z_1 = R_{ct} + \frac{1}{(i\omega + 1/R_1C_1)} \tag{49}$$

The comparison of the Z_1 expression (Eq. (49)) with that given by Eq. (37), leads to the following relationships for τ_1 and ρ_1 parameters

$$\tau_1 = \frac{1}{(1/R_1C_1 - R_{ct}/\rho_1)} \quad \text{and} \quad \rho_1 = -C_1R_{ct}^2 \tag{50}$$

In Figs. 12A and B the determined values of τ_1 and ρ_1 according to Eq. (50) are plotted upon the polarization potential and compared with the calculated ones using Eqs. (38) and (39), and the parameters depicted in Table 2. The experimental and simulated data have the same evolution shape against the potential. Nevertheless, with the B field the data are much lower than
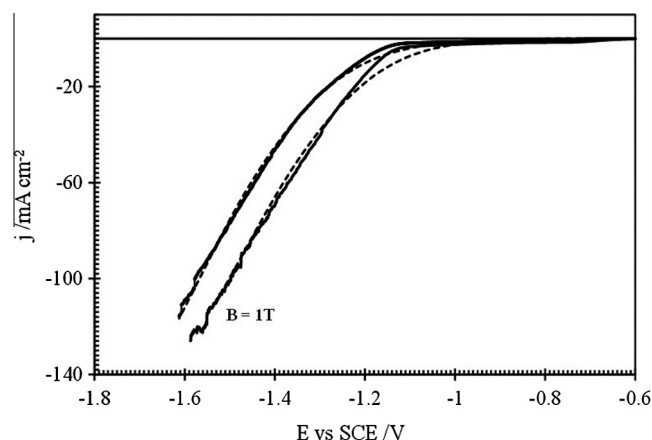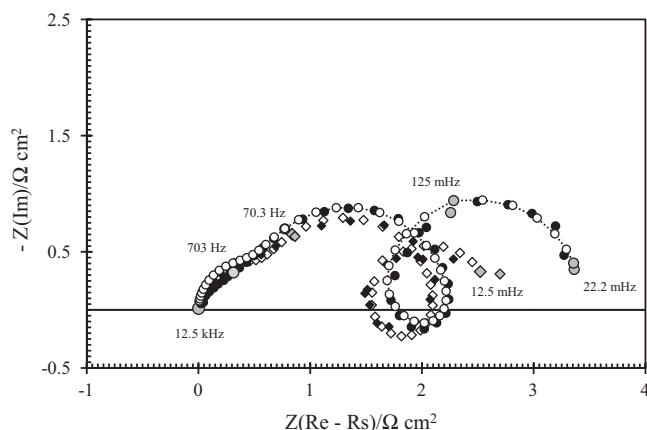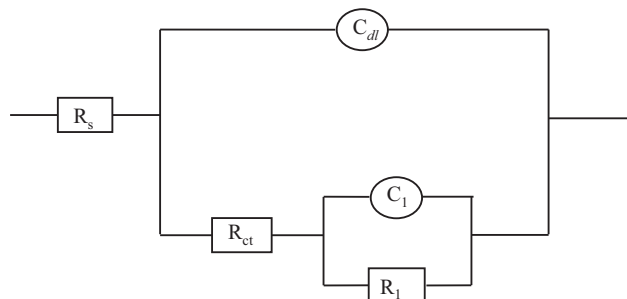

Fig. 9. Comparison of the experimental and calculated polarization curves without and with B = 1 T.

Fig. 10. Comparison of the experimental and calculated impedance diagrams. (●, ○): $B = 0$, (♦, ◊) $B = 0.75$ T. Full symbols: experimental data. Empty symbols: calculated impedance using the parameters values reported in Table 2.
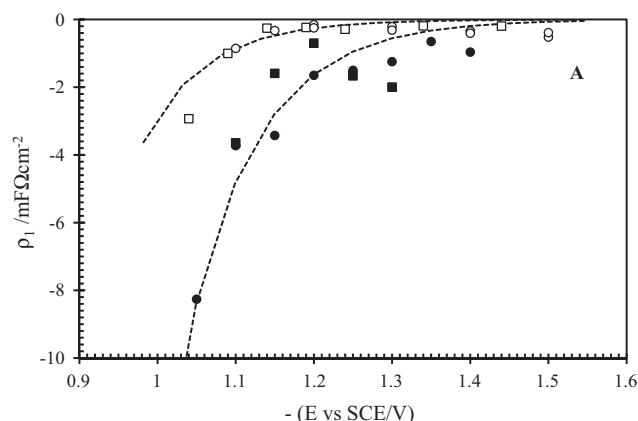

Fig. 11. Equivalent circuit composed of pure electric elements R_{ct}, C_{dl}, C_1 and R_1.

Fig. 12A. Variation of ρ_1 with respect to polarization potential. Vertical Pt electrode: (■): $B = 0$; (□): $B = 0.75$ T; vertical Ti electrode. (●): $B = 0$; (○): $B = 0.75$ T. $[Na_2MoO_4] = 0.05$ M; $[NiSO_4] = 0.5$ M & $[Na_3C_6H_5O_7] = 0.45$ M. pH = 6.2 & $T_b = 37\ °C$. The lines correspond to the calculated data using Eq. (38) and parameters values reported in Table 2.

Fig. 12B. Variation of the time constant τ_1 with respect to the polarization potential. Vertical Pt electrode: (■): $B = 0$; (□): $B = 0.75$ T; vertical Ti electrode. (●): $B = 0$; (○): $B = 0.75$ T. $[Na_2MoO_4] = 0.05$ M; $[NiSO_4] = 0.5$ M & $[Na_3C_6H_5O_7] = 0.45$ M. pH = 6.2 & $T_b = 37\ °C$. The lines correspond to the calculated data using Eq. (39) and parameters values reported in Table 2.

without the field indicating that the parameter ρ_1 seems to be very sensitive to the hydrodynamic conditions (Fig. 12A). Similar remarks may be drawn after comparison of the experimental and calculated data of the time constant τ_1 which exhibits slight linear decrease of $\log(\tau_1)$ against potential without and with $B = 0.75$ T (Fig. 12B). The experimental data are in good agreement with the model when the values reported in Table 2 are used. In all cases, under B field the magnitude τ_1 is much lower indicating that the adsorption equilibrium is relatively fast in comparison with the case when the B field was absent. This count either for Ti or Pt substrate used for Ni–Mo alloys deposition. Despite the great number of adjustable parameters, many of them exhibit reasonable statistical determination. It should be noticed that for the fitted values of b_i, Γ, m, D and δ reported in Table 2, the standard error never exceed 8%. However for $k_i°$ the standard errors may reach more than 19% in the case of $k_1°$ and $k_2°$. Indeed due to some probable drifts of the spectra resulting from hydrogen bubbling and surface development, the large errors of certain parameters shows that their determination is far from being accurate.

5.3. Charge transfer resistance

At fixed potential the $R_{ct}I$ product independency against B field indicates that according to Eq. (46), the R_{ct} resistance is inversely proportional to the limiting current density In addition if the electrodeposition process is under mass transport control the current generated by magnetic field is proportional to $B^{1/3}$ (Eqs. (1), (47) and Fig. 3A). Consequently, R_{ct} must be varied as $B^{-1/3}$ according to Eq. (48). In Fig. 13 typical R_{ct} vs $B^{-1/3}$ plot is reported for $E = -1.20$ vs SCE/V. This gives a constant value at $B = 0$ followed by straight line and confirms that R_{ct} varies linearly upon $B^{-1/3}$.
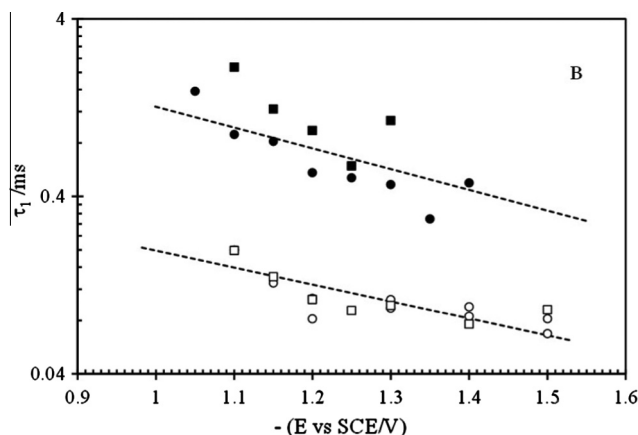
The fact that the line is not crossing the origin confirms that in this potential region Ni–Mo alloys electrodeposition is under mixed control (kinetics and mass transport), and shows that the data are in good agreement with Eq. (48).

5.4. Polarization resistance

According to [36], under MHD convection control, the expression of diffusion impedance, Z_d, given by Eq. (42) can by written in the following form

$$Z_d = R_{ct} \frac{1}{H(\sigma)} \frac{\chi}{\left(kBC^*D^2d^5\right)^{1/3}} \tag{51}$$

where $H(\sigma)$ is a hydrodynamic transfer function which depends on the dimensionless frequency σ [36]. In Eq. (51), the term χ is a variable function containing the kinetic parameters and corresponds to

$$\chi = \frac{1}{nF}\left(\frac{\partial j}{\partial C}\right) \tag{52}$$
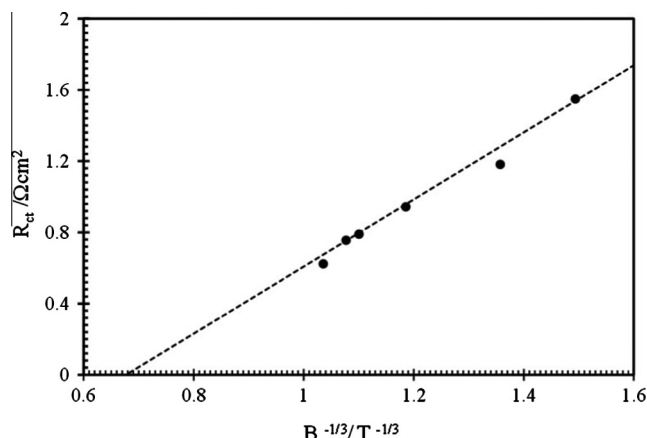
Fig. 13. Variation of the charge transfer resistance R_{ct}, against $B^{-1/3}$ at $E = -1.20$ vs SCE/V and Pt vertical electrode. [Na_2MoO_4] = 0.05 M; [$NiSO_4$] = 0.5 M & [$Na_3C_6H_5$-O_7] = 0.45 M. pH = 6.2 & T_b = 37 °C.

When the frequency tends to zero ($\sigma \to 0$), the hydrodynamic transfer function tends to a constant value $H(0) = 0.8075$ and Z_d corresponds to its low frequency limit, R_d, given by

$$R_d = \frac{1}{0.8075nF} \frac{R_{ct}}{\left(\kappa BCD^2 d^5\right)^{1/3}} \left(\frac{\partial j}{\partial C}\right) \tag{53}$$

In the polarization potential range, where the Ni–Mo electrodeposition process is predominantly under mass transport control, the diffusion resistance R_d has a high contribution in the polarization resistance value R_p. In addition, if we take into account that R_{ct} is proportional to $B^{-1/3}$ as it was shown before in Fig. 13 and in Eq. (48), from Eq. (53) one may assume that R_p varies linearly with $B^{-2/3}$. Fig. 14 reports the plot of R_p against $B^{-2/3}$ for $E = -1.20$ vs SCE/V. It is obvious that a straight line is obtained when the diffusion process is predominant. This means that our assumptions are verified and shows that in the polarization region where Ni–Mo deposition is under mass transport control the polarization resistance values may be controlled by magnetic field intensity. It must be noticed that the polarization resistance R_p, corresponds to sum of the contribution of charge transfer and mass transport processes. With magnetic field, only the mass transport phenomenon is modified by magnetic convection and the R_p vs $B^{-2/3}$ straight line does not cross the origin.

6. Conclusions

The following conclusions can be drawn from this work, in which the Ni–Mo alloys electrodeposition kinetics under an external magnetic field B was studied using polarization curves and electrochemical impedance methods:

– an increase of the cathodic current density was observed in the potential domain were the Ni–Mo alloys electrodeposition is under mass transport control,
– the EIS diagrams evolution with magnetic field is in accordance with the stationary evolution with slight increase of the double layer capacitance associated to the modifications of the deposits real surface area,
– at constant potential, the charge transfer resistance and the polarization resistance decrease according to the MHD convection theory (i.e. $R_{ct} \propto B^{-1/3}$ and $R_p \propto B^{-2/3}$),
– a reaction path for Ni–Mo alloys electrodeposition from citric bath is tentatively developed and compared to experimental data. The proposed model accurately accounts for the mean features of EIS and polarization data, with and without magnetic field.
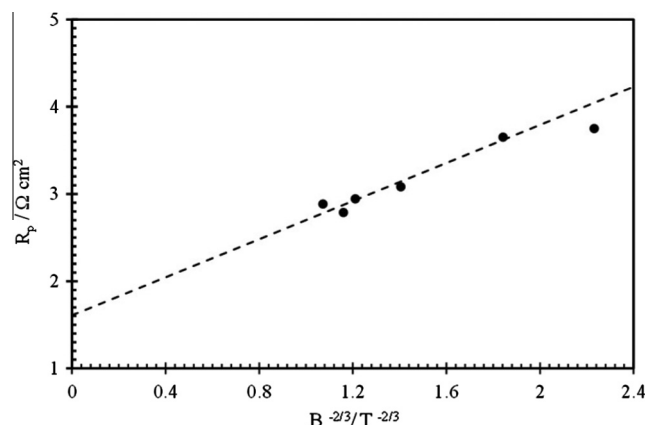
Fig. 14. Variation of the polarization resistance R_p, against $B^{-2/3}$ at $E = -1.20$ vs SCE/V and Pt vertical electrode. [Na_2MoO_4] = 0.05 M; [$NiSO_4$] = 0.5 M & [$Na_3C_6H_5$-O_7] = 0.45 M. pH = 6.2 & T_b = 37 °C.

Conflict of interest

There is no conflict of interest.

References

[1] E. Navarro-Flores, Z. Chong, S. Omanovic, J. Mol. Catal. A Chem. 226 (2005) 179.
[2] L. Birry, A. Lasia, J. Appl. Electrochem. 34 (2004) 735.
[3] S. Martinez, M. Metikos-Hukovic, L. Valek, J. Mol. Catal. A: Chem. 245 (2006) 114.
[4] O. Aaboubi, Int. J. Hydrogen Energy 36 (2011) 4702.
[5] H.B. Hassan, Z. Abdel Hamid, Surf. Interface Anal. 45 (2013) 1135.
[6] E. Chassaing, V. Quang, R. Wiart, J. Appl. Electrochem. 19 (1989) 839.
[7] E.J. Podlaha, D. Landolt, J. Electrochem. Soc. 143 (1996) 893.
[8] A. Marlot, P. Kern, D. Landolt, Electrochem. Acta 48 (2002) 29.
[9] E. Beltowska-Lehman, P. Indyka, Thin Solid Films 520 (2012) 2046.
[10] S. Sun, E.J. Podlaha, J. Electrochem. Soc. 159 (2013) D97.
[11] L.S. Sanches, S.H. Domingues, C.E.B. Marino, L.H. Mascaro, Electrochem. Commun. 6 (2004) 543.
[12] E. Gomez, E. Pellicer, E. Vallés, J. Electroanal. Chem. 580 (2005) 222.
[13] S. Yagi, A. Kawakami, K. Murase1, Y. Awakura, Electrochem. Acta 52 (2007) 6041.
[14] O. Devos, A. Olivier, J.-P. Chopart, O. Aaboubi, G. Maurin, J. Electrochem. Soc. 145 (1998) 401.
[15] I. Tabakovic, V. Inturi, S. Riemer, J. Electrochem. Soc. 149 (2002) C18.
[16] K. Msellak, J.-P. Chopart, O. Jbara, O. Aaboubi, J. Amblard, J. Mag. Mag. Mater. 281 (2004) 295.
[17] A. Krause, C. Hamann, M. Uhlemann, A. Gebert, L. Schultz, J. Mag. Mag. Mater. 290–291 (2005) 261.
[18] O. Aaboubi, J. Douglade, P. Zabinski, J.-P. Chopart, Magnetohydrodynamics 48 (2012) 271.
[19] M. Uhlemann, K. Tschulik, A. Gebert, G. Mutschke, J. Fröhlich, A. Bund, X. Yang, K. Eckert, Eur. Phys. J. Special Top. 220 (2013) 287.
[20] V. Georgescu, M. Daub, Surf. Sci. 600 (2006) 4195.
[21] R. Aogaki, K. Fueki, T. Mukaibo, Denki Kagaku 44 (1976) 89.
[22] T.Z. Fahidy, J. Appl. Electrochem. 13 (1983) 553.
[23] O. Aaboubi, J.-P. Chopart, J. Douglade, A. Olivier, C. Gabrielli, B. Tribollet, J. Electrochem. Soc. 137 (1990) 1796.
[24] N. Pamme, Lab. Chip. 6 (2006) 24.
[25] N. Leventis, X. Gao, J. Am. Chem. Soc. 124 (2002) 1079.
[26] G.J. Brug, A.L.G. Ven den Eeden, M. Sluyters-Rebach, J. Sluyters, J. Electroanal. Chem. 176 (1984) 275.
[27] B.A. Boukamp, Solid State Ionics 169 (2004) 65.
[28] B. Hirschorn, M.E. Orazem, B. Tribollet, V. Vivier, I. Frateur, M. Musiani, J. Electrochem. Soc. 157 (2010) C452.
[29] E. Beltowska-Lehman, A. Bigos, P. Indyka, M. Kot, Surf. Coat. Technol. 211 (2012) 67.
[30] P. Fricoteaux, A. Olivier, P. Delmas, J. Electrochem. Soc. 157 (1992) C452.
[31] O. Devos, O. Aaboubi, J.-P. Chopart, A. Olivier, C. Gabrielli, B. Tribollet, J. Phys. Chem. A 104 (1999) 1544.
[32] V.G. Levich, Physicochemical Hydrodynamics, Prentice Hall, New York, 1962.
[33] M.E. Lago, M.A. Patrick, A.A. Wragg, J. Braz. Chem. Soc. 6 (1995) 105.
[34] S. Legeai, M. Chatelut, O. Vittori, J.-P. Chopart, O. Aaboubi, Electrochim. Acta 50 (2004) 51.
[35] I. Citti, O. Aaboubi, J.-P. Chopart, C. Gabrielli, A. Olivier, B. Tribollet, J. Electrochem. Soc. 144 (1997) 2263.
[36] O. Devos, O. Aaboubi, J.-P. Chopart, A. Olivier, C. Gabrielli, B. Tribollet, J. Phys. Chem. B 103 (1999) 496.
[37] O. Aaboubi, 216th ECS Meeting, Vienna, Austria, 2009, Abstr. I2-3026.